



## Detection and formation mechanisms of secondary nanoplastic released from drinking water bottles

Anna Winkler<sup>a,1</sup>, Francesco Fumagalli<sup>b,1</sup>, Claudia Cella<sup>b</sup>, Douglas Gilliland<sup>b</sup>, Paolo Tremolada<sup>a</sup>, Andrea Valsesia<sup>b,\*</sup>

<sup>a</sup> Department of Environmental Science and Policy, University of Milan, Via Celoria 26, Milan 20133, Italy

<sup>b</sup> European Commission, Joint Research Center (JRC), Ispra, Italy

### ARTICLE INFO

#### Keywords:

Secondary nanoplastics  
Analytical methods  
Quantification methods  
Drinking water  
Single particle extinction and scattering  
Raman spectroscopy

### ABSTRACT

Since nanoplastics are currently considered potentially hazardous to the environment and human health, reliability of studies on nanoplastic exposure becomes crucial. However, analytical challenges limit our understanding of their formation and detection, thus hampering their biological interactions assessment. Here we provide a combined approach to quantitatively and qualitatively detect the release of nanoplastics in water matrix and, in particular, to measure direct exposure of consumers by simulated use of drinking water plastic bottles. We measured that the polyethylene sealing of the bottles released particles with a size distribution ranging from few hundreds nanometers up to about one micron and estimated a mass release in the order of few tenths of nanograms per opening/closing cycle. We observe that mechanical stress alters the physical-chemical characteristics of the generated secondary nanoplastics and degrades the material properties compared to the original bulk source, thus complicating their spectroscopic chemical identification. Our findings demonstrate that understanding material degradation processes is therefore crucial for identifying and quantifying nanoplastics in real samples. Moreover, methods allowing quantitative studies on the release of nanoplastic as a source of exposure are considered essential for proper assessment of their potential health hazards and to promote improvements in consumer products plastic packaging design.

### 1. Introduction

Although the growing concern about plastic micro- (MP) and nanoparticles (NP) pervasive diffusion in the environment and human's food-chain, conclusive evidence of their potential health hazards is not yet available (Lim, 2021; Mitrano et al., 2021). NP, defined in this work as secondary sub-micron objects resulting from fragmentation of plastic materials and exhibiting colloidal behaviour (Gigault et al., 2021), are the most difficult to detect but potentially the most harmful particles since they are small enough to interact at a cellular level. To date, a definitive statement on NP toxicity cannot be provided since it is agreed that insufficient scientific evidence is available about the level of exposure and their interaction with organisms (Zhang et al., 2020). This

is not surprising considering how little is currently known about the physical-chemical properties of secondary nanoplastic debris. Depending on the measurement metric used and NP model characteristics (Blanco et al., 2021; Gigault et al., 2021; Lin et al., 2019), toxicity experiments can lead to varying outcomes (Kögel et al., 2020). Despite these knowledge gaps, uptake of MP/NP via direct exposure from consumer goods is undisputed. Confirmed sources include both foods and beverages products (Fadare et al., 2020; Laborda et al., 2021), such as bottled water (Cox et al., 2019; Shruti et al., 2021) with focus on particulates originating from plastic packaging. Recently, a few studies have confirmed the release of MP/NP by food packaging, identifying different degradation pathways and unintentional sources of human consumption of secondary MP/NP. Mechanical stress to HDPE bottle

**Abbreviations:** EPDM, ethylene-propylene-diene-monomer rubber; FTIR-ATR, attenuated total reflection - fourier-transform infrared spectroscopy; HDPE, high density polyethylene; LDPE, low density polyethylene; mQ-H<sub>2</sub>O, milli-Q ultrapure water; PE, polyethylene; PET, poly(ethylene terephthalate); MP, microplastics; NP, nanoplastics; PS, polystyrene; SBR, styrene-butadiene rubber; SEM-EDS, scanning electron microscopy - energy dispersive X-ray spectroscopy; SPES, single particle extinction and scattering, XLPE, cross-linked polyethylene; XPS, X-ray photoelectron spectroscopy; XRD, X-ray diffraction analysis.

\* Corresponding author.

E-mail address: [andrea.valsesia@ec.europa.eu](mailto:andrea.valsesia@ec.europa.eu) (A. Valsesia).

<sup>1</sup> These authors contributed equally to this work.

<https://doi.org/10.1016/j.watres.2022.118848>

Received 12 January 2022; Received in revised form 6 July 2022; Accepted 9 July 2022

Available online 10 July 2022

0043-1354/© 2022 The Authors. Published by Elsevier Ltd. This is an open access article under the CC BY license (<http://creativecommons.org/licenses/by/4.0/>).

screw caps, i.e., opening and closing a drinking water bottle, has been observed to release MP and identified as potential ingestion source through transfer via oral exposure (Weisser et al., 2021; Winkler et al., 2019). Thermal stress from heat has also been confirmed to release MPs/NPs from food packaging, e.g., when brewing a teabags (consisting of nylon and PET) (Cella et al., 2022; Hernandez et al., 2019), cooking rice in PE cooking bags (Cella et al., 2022) or hot liquids in paper cups coated with PE films (Ranjan et al., 2021) and other plastic materials holding hot liquids (Liu et al., 2022; Schwabl, 2020). Also, thermal stress through freezing had been verified to release MP/NP, as recently observed for ice-cube bags (Cella et al., 2022). Contamination of MP/NP can also occur by simple contact of food product with the plastic packaging, as observed for, e.g., meat in extruded polystyrene trays (Kedzierski et al., 2020) or transfer from plastic take-out containers (Du et al., 2020). Regulating bodies have thus begun discussing safety assessment actions for occurrence, analysis and toxicity of NPs in food and drinking water (Allan et al., 2021). While knowledge about MP detection is increasing, NP studies are still lagging behind since the development of comprehensive detection strategies proved challenging. Mass-spectroscopy based techniques can identify the presence of plastics in the ng range (Materić et al., 2020; Ter Halle et al., 2017) but lack characterization capabilities of microscopic methods. While diffraction-limited spectroscopic identification/quantification techniques (e.g.,  $\mu$ -Raman) can in principle resolve sub-micron individual particles in laboratory conditions (Gillibert et al., 2019), practical issues with matrix reduction and particle concentration from real samples greatly complicate the analysis (Valsesia et al., 2021). Often, a multi-technique approach is needed to obtain the necessary information on chemical character, shape, size distribution, and concentration (Schwaferts et al., 2019; Ter Halle et al., 2017). Remarkably, the approach proposed in Schwaferts et al. (2019) combines high-resolution imaging techniques (Electron Microscopy), chemical identification techniques (vibrational spectroscopies or mass spectroscopies) and particle scattering techniques for a complete characterization of polymeric nanoparticles. Among the different particle scattering techniques Single Particle Extinction and Scattering (SPES) has been successfully used for the counting and identification of polymeric nanoparticles in different media (Potenza et al., 2015; Sanvito et al., 2017). Moreover, physico-chemical mechanisms occurring during top-down formation of secondary NP from larger particles are mainly responsible for the observed heterogeneity in their material properties, transfer pathways and reactivity (Hamzah et al., 2018; Liu et al., 2020). Together with other stressors such as photodegradation and biodegradation, realistic degradation-induced modifications must be taken into account while developing reliable analytical detection methods since the use of overly simplified laboratory models may lead to non-representative conclusions.

In this study, we will describe a multi-technique analytical methodology for NP detection, identification and size distribution measurement as applied to the analysis of sub-micron particulate release from drinking water bottles under realistic use conditions. Furthermore, we identify and discuss NP physical-chemical properties modifications occurring during secondary formation pathways and their impact on particulate identification and quantification. Understanding the differences between secondary nano-objects and their primary macro sources can play a crucial role in designing effective biological interaction NP models and experiments.

## 2. Materials and methods

### 2.1. Study design

The release of MP/NP particles from PET-bottlenecks and HDPE cap material was determined after an opening and closing procedure to mimic the mechanical stress caused by using a bottle. Quantity, chemical and size range analyses of released particles were performed by

Single Particle Extinction and Scattering (SPES), X-ray photoelectron spectroscopy (XPS), Scanning Electron Microscopy (SEM),  $\mu$ -Raman spectroscopy, Fourier-transform infrared Attenuated total reflectance (FTIR-ATR) and  $\mu$ -FTIR spectroscopy. Although all the methods are non-destructive, the analyses with SEM, XPS,  $\mu$ -Raman and  $\mu$ -FTIR require specific filters to provide optimal conditions for clear results, which made the use of a new set of prepared samples for these instruments necessary. The experimental process is described below.

### 2.2. Sample processing

For sampling material preparation, mineral water bottles (0.5 L) from local supermarkets were purchased, and the outer surface was cleaned with ethanol. The bottle itself consisted of transparent PET, and the cap was made of white HDPE material as indicated by the manufacturer and verified via FTIR-ATR measurements. To apply mechanical stress, one bottle was opened and closed 1, 10, and 50 times manually without fully removing the cap during each open-close cycle. The water content was previously released by cutting the bottle base with a cutter. When the bottle was first opened, the security ring detached from the cap and remained loose at the lower end of the bottleneck. To detach the MP/NP released from the PET bottleneck surface and HDPE cap that passed over to the bottleneck due to the treatment, the cap was removed. Particles were rinsed off the bottleneck by immersing it head down into a small glass beaker containing 15 mL Milli-Q ultrapure water (mQ-H<sub>2</sub>O) so that only the bottleneck was entirely covered. The bottleneck was left in the solution for 3 min while gently agitating. For the analysis with SPES, the bottle was removed and the beaker transported to the instrument where the solution was directly analysed. The same solutions were then used for  $\mu$ -Raman and SEM analysis after two concentration steps. The concentration of the sample solution facilitates the analysis of volumes with low MP/NP concentration for spectroscopic and microscopic analyses by reducing the area of analysis to a small droplet on a suitable surface. The first concentration of the solutions was performed by applying an Amicon Ultra 25 mL Centrifugal Filter having a molecular weight cut-off of 100,000 kDa. The solution was centrifuged for 2 min at max speed (4500 x g, swing-bucket rotor), leaving the residual sample in the top part of the Amicon unit. The sample reservoir contains the concentrate, of which 500  $\mu$ L were collected using a pipette. The concentrate was transferred into an Amicon Ultra 0.5 mL Centrifugal Filter having a molecular weight cut-off of 10,000 kDa. The sample was centrifuged for 2 min at max speed (21,130 x g, fixed angle), resulting in a concentrated solution of 25  $\mu$ L. Of the final concentrate, 1  $\mu$ L were taken with a pipette and spotted on silicon chips for Raman analysis. Another 1  $\mu$ L were spotted on cleaned flat silicon chips for SEM analysis. Samples were dried before the analysis. In addition, the release of microplastic particles from the bottle material was tested by  $\mu$ -FTIR spectroscopy. An additional bottle was opened/closed 50 times, and the bottleneck immersed in 0.1% sodium dodecyl sulphate (SDS) solution to aid hydrophobic particles recovery from the solution. However, since the analysis of one bottle opened/closed 50 times could identify only one PE particle, 390  $\mu$ m in size (Fig. S1), no further replicates were considered. For the sake of completeness, the method is described further below. Results and details of  $\mu$ -FTIR analysis (of the detected PE micro-particle) are reported in the SI, Fig. S1.

### 2.3. Quality control

Before proceeding with the experiments, it was necessary to verify that plastic particles potentially released on the bottleneck were indeed rinsed off from the bottle by immersion in mQ-H<sub>2</sub>O for 3 min, without the use of additional solvents. Accordingly, SEM images (JEOL JSM-IT500) of the neck of two further bottles opened/closed 50 times were taken to count particles applying a semi-quantitative approach. One bottleneck before and one after the immersion was removed from the bottle body with a scalpel and mounted on aluminium stubs. For each

bottleneck, three SEM images with a magnification of 50 X were taken on a vertical line from the top to the bottom edge of the bottleneck surface. The SEM images were processed to count detected microparticles on bottlenecks before and after the immersion in mQ-H<sub>2</sub>O. Operating conditions were: accelerating voltage 20 kV, probe current 80 mA, and working distance 15.7–17.6 mm. The semi-quantitative analysis on the analysed surface area of the bottleneck revealed four particles (170–550 µm in size) before and no particles after the immersion of the bottle (Fig. S2), confirming the successful removal of particles from the bottle into the water. EDS analysis of these particles resulted in an elemental composition of 100% carbon (Fig. S3), which is consistent with HDPE and, therefore, suggesting particle derived from the cap material. We included procedural lab blanks consisting of 15 µL mQ-H<sub>2</sub>O, which underwent the same processes as the samples. The “blank” sample was placed in another beaker close to the soaking beaker for all the time needed to process the 50 times sample. Then it underwent the same processes. Moreover, pristine mQ-H<sub>2</sub>O directly from the distributor was analysed by SPES for comparison. Additionally, we cryomilled cap material (HDPE) of the same bottle brand as reference material for µ-Raman spectroscopy to simulate effects of mechanical stress (irregular particles rather than micro- and nanobeads). Cap material was cut into smaller pieces and placed in the sample holders (polycarbonate sample holder) of the cryomill (Cryomill 6875 Freezer/Mill® Spex) together with NaCl to enhance grinding. Milling conditions were: 20 min cooling time, nine cycles of 2 min and 2 min rest, repeated four times. All glass wear and metal cutlery were cleaned with washing detergent and rinsed with fresh mQ-H<sub>2</sub>O. Laboratory surfaces on which the preparations were performed were covered with a layer of aluminium foil. All persons wore cotton lab coats or non-synthetic clothes and washed their hands frequently.

#### 2.4. Single particle extinction and scattering

For the determination of particle number and size distribution, single particle extinction and scattering analysis was performed using the CLASSIZER™ ONE (EOS S.r.l., Milan, Italy), equipped with a red light diode ( $\lambda = 640$  nm, power < 50 mW). This light scattering method enables the analysis, classification and counting of single particles in fluids based on their optical properties. Briefly, particles passing the focal region of a light beam transmit and scatter light that can be collected onto a sensor placed in the far-field of the laser beam. This can give a measure of the complex amplitude of the forward scattered field via a self-reference interferometric scheme (Potenza et al., 2015; Villa et al., 2016). The scattered field amplitude depends on several important nanoparticles' characteristics (i.e., size, refractive index ( $n$ ) and shape) that can be analysed with the technique. In this work, we focus on the size distribution and particle concentration. The results are presented in a 2D histogram having as X- and Y-axis the complex scattered field components ( $Re[S(O)]$ ,  $Im[S(O)]$ ) and as Z-axis the concentration (counts·bin<sup>-1</sup>·cm<sup>-3</sup>) within each 2D-bin in the complex  $S(O)$  plane (Potenza et al., 2015). In the case of dielectric particles and under the assumption of spherical shape, both size and  $n$  can be simultaneously and unambiguously determined from the  $S(O)$  raw data thanks to the Mie scattering calculations. Even in the case of non-spherical particle shapes, and for particles aspect ratios (AR) lower than 2–3 (Chyacutelek et al., 1976), the spherical approximation leads to a precision over the refractive index measurement better than 10%. Therefore, the evaluation of the numerical size distribution of the whole sample was obtained by applying the dielectric sphere model. The lower and upper detection limit for dielectric material such as polymers is 200 nm to 20 µm. The instrument was operated with a constant flow of 4 mL per minute. Total analysed volume varied from 66 to 78 mL, which was obtained by fluxing the sample multiple times to ensure a sufficient number of detectable particles. Since the method is non-invasive and non-destructive, the suspension returned into the sample beaker and could be further used for µ-Raman and SEM investigation. In addition,

by approaching the analysis with the Mean Field Approximation (Bohren and Huffman, 1998; Chýlek et al., 1988) and the Lorentz-Mie method, an average filling factor evaluation was performed to detect signs of agglomeration or indication for a shape similar to a ball of fibre or a porous particle. The average filling factor analysis reports the filling percentage inside the detected particle of the bulk expected material (HDPE or PET in our analysis). Analyses were performed by the software version ClassizerONE S1.4.34.

#### 2.5. Micro-Raman spectroscopy

Raman analysis was performed on the concentrated samples drop-casted onto the silicon chips. The samples on the chips were analysed using a WITec Confocal Raman Microscope (Witec, Ulm, Germany), equipped with a  $\lambda = 532$  nm laser. The scan resolution was 200 nm and the integration time per pixel was 5 s. A 100 × magnification object was used with numerical aperture of 1.25. Univariate analysis of the hyperspectral images was performed using the Witec instrument software (Witec Suite 5) by integration of the spectra corresponding to the spectral bands between 2800–3100 cm<sup>-1</sup> assigned to the C-H stretching of polymers. Cosmic Rays Removal and baseline correction tools were applied to the spectra before univariate analysis. The lowest detection limit of single isolated nanoparticles for this instrument was 0.5 µm (using commercial PS beads, PolyScience Inc). The Raman spectra were fitted with an appropriate number of Voigt functions for each spectral band using a nonlinear, least-squares Levenberg-Marquardt regression method. Fitting parameters were peak centres, FWHM, areas for each peak and the common linear baseline. Peak positions were constrained  $\pm 5$  cm<sup>-1</sup> using literature references from HDPE (Bentley and Hendra, 1995; Gaston et al., 2018; Snyder et al., 1978; Zhang et al., 1997). The uncertainty of peak positions and areas were less than  $\pm 0.5$  cm<sup>-1</sup> and  $\pm 10\%$ , respectively. Mass fractions of crystalline domains, *trans* and amorphous conformers were calculated according to the method originally suggested by Strobl et al. (Rull et al., 1993; Strobl and Hagedorn, 1978) and later adopted by several authors (Migler et al., 2015) describing PE using a three phases model (amorphous, orthorhombic crystalline and non-crystalline consecutive *trans* conformers, NCCT). In the method, the intensity of the  $\tau(\text{CH}_2)$  twist vibration band around 1300 cm<sup>-1</sup> is used as internal normalisation standard. The band intensity ratio with its component's intensities 1298 cm<sup>-1</sup> and 1305 cm<sup>-1</sup> yields the *trans* and amorphous conformers' mass fractions. The reference band ratio with the 1416 cm<sup>-1</sup> peak (interchain interactions from  $\delta(\text{CH}_2) + \omega(\text{CH}_2)$  vibrations) can then be used to differentiate the mass fraction contribution from the orthorhombic crystalline regions from the non-crystalline consecutive *trans* conformers ( $\chi_{\text{orthorhombic}} = \chi_{\text{trans}} - \chi_{\text{NCCT}}$ ). For comparison, reference spectra acquired on the bottles bulk materials are shown in Fig. S4.

#### 2.6. Scanning electron microscopy

Scanning electron microscopy (SEM) images of concentrated samples on silicon chips were recorded using a Thermofisher, FEI, NOVA 600i electron microscope operating at an acceleration of 2 kV and magnification of 65X at a working distance varying from 4 to 7 mm. Further high-resolution SEM images were acquired from different sample areas with varying magnifications (1000–16000 X). EDS spectroscopy and mapping were carried out in a Nova 600i Nanolab (Thermofisher, Eindhoven, The Netherlands) equipped with an EDS system for elemental analysis (EDAX Inc, Mahwah, NJ, USA). The EDS system mounts an Octane Elect Plus x-rays detector. Typical EDS maps and spectra were acquired using Acceleration Voltage values between 10 and 25 kV, with Take Off angle of 35° and Dwell Time of 200 ms.

#### 2.7. X-ray photoelectron spectroscopy

XPS measurements were performed with an Axis Ultra spectrometer

(Kratos, Manchester, UK), using a  $K\alpha$  Al monochromatic source ( $h\nu = 1486.6$  eV) operating at 150 W and an X-ray spot size of  $400 \times 700$   $\mu\text{m}^2$  in the hybrid mode. Large spot sizes allowed to obtain good S/N ratios in recorded spectra, even if they can introduce drawbacks related to possible substrate contribution and require suitable film deposition method. In order to overcome these issues, we deposited filtered particulate films by drop/casting, and we used Teflon strips as substrates. Sample preparation procedures established in literature were followed for solid (Bañuls-Ciscar et al., 2020) and nanoparticles (Bennet et al., 2020) surfaces, respectively. The residual pressure of the analysis chamber during the analysis was less than  $8 \times 10^{-9}$  Torr. For each sample, both survey spectra (0–1150 eV, pass energy 80 eV) and high-resolution spectra (pass energy at 40 eV) were recorded. Surface charge was compensated by a magnetic charge compensation system, and the energy scale was calibrated by setting the C 1s hydrocarbon peak to 285.00 eV in binding energy (Baer and Engelhard, 2010; Shard, 2020). The data were processed using Vision2 software (Kratos Analytical, UK), and the analysis of the XPS peaks was carried out using a commercial software package (CasaXPS v2.3.18PR1, Casa Software, Ltd., UK). Peak fitting was performed with no preliminary smoothing. Symmetric Gaussian–Lorentzian (70% Gaussian and 30% Lorentzian) product functions were used to approximate the line shapes of the fitting components after a 3-parameters Tougaard-type background subtraction. Concentrated samples were dispersed in mQ-H<sub>2</sub>O and drop-casted on clean Teflon substrates. The use of Teflon substrate allows minimizing the uncertainties in the stoichiometric evaluation of the C content of the surface, mainly due to adventitious hydrocarbon contamination. This is especially critical in case of low thicknesses of the analysed films. The high binding energy shift of electrons originating from C-F bonds and the precisely known Teflon stoichiometry allows separating with high confidence the substrate and sample contributions during the C 1s peak fitting. Accordingly, Teflon substrate contribution to the C 1s signal was not considered in the elemental quantification of the sample. For comparison, reference spectra acquired on the bottles bulk materials are shown in Fig. S5.

## 2.8. Micro-FTIR spectroscopy

For the preparation of the  $\mu$ -FTIR analysis, the particles were removed from the bottleneck as described above. The solution was transferred into a standard vacuum-filtration apparatus and the beaker rinsed with 5 mL mQ-H<sub>2</sub>O. The filter membrane was Whatman® Anodisc inorganic filter membrane (diam. 13 mm) with a nominal pore size of 0.1  $\mu\text{m}$ . The membrane is composed of a high purity alumina porous matrix. After filtration, the membrane was placed in a clean, covered petri dish for drying. Micro-FTIR microscopy was performed using a Bruker Infrared Imaging Microscope. Since the surface of the filters is transparent for IR-radiation with wavenumbers above  $1300$   $\text{cm}^{-1}$ , measurement of all particles  $> 10$   $\mu\text{m}$  (approximate detection limit for this instrument in our configuration) was carried out in transmission mode in a wavenumber range of  $4000 - 1300$   $\text{cm}^{-1}$ . Transmission mode allowed for the determination of the particle, minimising the interference of a potential surface cover layer or soiling. The measurements were controlled by native Bruker OPUS8.5 software. For each experiment, either the full or, in the case of blanks, at least  $\frac{1}{4}$  of the surface area of the filter was analysed. A total of 64 scans were taken for each spectrum, with a spectral resolution of  $4$   $\text{cm}^{-1}$ . The IR absorbance was compared with spectra generated by reference material obtained from PET from bottlenecks and HDPE from bottle caps and with internal OPUS spectral library. For comparison, reference spectra acquired on the bottles bulk materials are shown in Fig. S6. Both sides of the bottle body and screw cap were measured to expose eventual occurrence of oxidation due to weathering/ageing of the polymeric materials (Bañuls-Ciscar et al., 2020) in the bottle. ATR-FTIR analysis shows no differences between the two surfaces of the bottle components (see Fig. S7).

## 2.9. Data analysis

Origin, CasaXPS and Microsoft Excel were used for data analysis. Origin and Inkscape were used for exporting data graphs.

## 3. Results and discussion

### 3.1. Morphological and chemical analysis

The release of MP/NP particles from commercial drinking water bottles was determined after several opening-closing cycles (1, 10, and 50 times) to mimic product (re)utilisation. The bottleneck-cap system (made of polyethylene terephthalate, PET, and polyethylene, PE, respectively, as stated by the manufacturer and verified via FTIR-ATR measurements) was rinsed with mQ-H<sub>2</sub>O after opening/closing cycles to recover released particulate. Care was taken to ensure efficient recovery and to avoid contamination from external sources. Chemical and size distribution analyses of released particles were performed combining Scanning Electron Microscopy (SEM), Single Particle Extinction and Scattering (SPES) (Potenza et al., 2015), X-ray photoelectron spectroscopy (XPS),  $\mu$ -Raman and  $\mu$ -Fourier-transform infrared (FTIR) spectroscopy. For SPES, that allows outlining particle size distribution and concentration, and  $\mu$ -FTIR measurements the rinsing water was analysed directly while for other techniques the solution was centrifugally filtered (at  $10^4$  kDa cut-off) and concentrated on a Si-chip surface. Qualitative SEM images analysis show that the amount of residual particulate recovered from the neck of water bottles after simulated use deviates from the procedural blank and increases with the number of opening/closing cycles (Fig. 1b–d), indicating an accumulation of particles whose approximate size range was well below  $5$   $\mu\text{m}$  (Fig. 1e–h). SEM/EDS elemental composition analysis on recovered particles showed almost exclusively carbon with the measured O/C ratio being close to zero (Figs. S2 and S3). This observation is compatible with common commodity thermoplastics such as PE (i.e., bottle cap material), PP, and PS, and with some synthetic elastomers' compositions (e.g., SBR, styrene-butadiene rubber; EPDM, ethylene-propylene-diene-monomer rubber) but not with PET (i.e., bottle material). Chemical identification of sub-micron particles via EDS is complicated due to increasing interference from surface oxidation (Gniadek and Dąbrowska, 2019) and matrix contaminations (Valsesia et al., 2021). Moreover, the size range of the observed residual particulate lies below the detection limit of  $\mu$ -FTIR spectrometers (Facchetti et al., 2020; Galafassi et al., 2021; Schymanski et al., 2018), as already observed in previous investigations on similar systems (Winkler et al., 2019).

Accordingly,  $\mu$ -FTIR analysis of the unfiltered rinsing water did not result in any statistically relevant PE or PET particle detection, even though some large PE objects were occasionally detected (Fig. S1). An XPS study was conducted on both the recovered particulates in the nano-range and the cleaved HDPE cap in order to chemically identify the materials through their elemental composition and stoichiometric ratios (Fig. 2, Tables S1 and S2). In fact, in the HDPE spectrum (Fig. 2c), the asymmetric line shape of the main C-C, C-H component can be used for chemical identification since it can be reliably fitted using the four symmetric C-H stretch vibrational components typical of PE (Beamson et al., 1991) However, the nanoparticulate O/C elemental ratio exhibits a six-fold increase with respect to the cap material ( $O/C_{HDPEcap} = [6.5 \pm 1.8] \%$ ;  $O/C_{NP} = [35.7 \pm 3.3] \%$ ), thus making the chemical identification based on stoichiometric ratios quite problematic. In addition, this increased surface oxidation (Fig. 2e, Table S2) in the nanoparticle spectrum resulted in a large overlap between the C-O components and the high binding energy tail of the C-C, C-H component, effectively making a univocal deconvolution of vibrational C-H components not feasible.

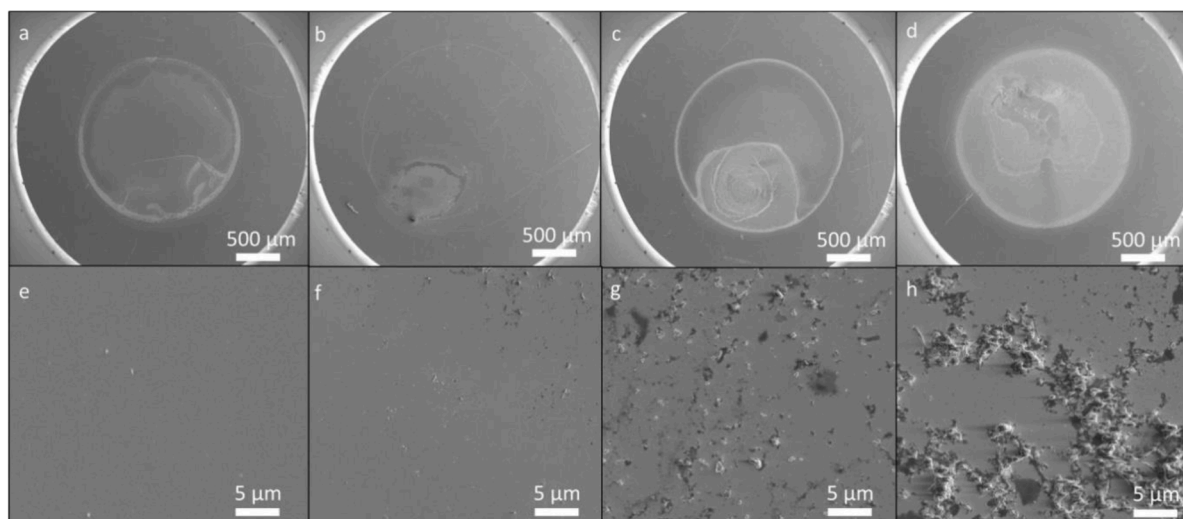


**Fig. 1.** Microscopic analysis of the nanoparticulate released from water bottles. SEM images of concentrated particulates dried on silicon chips. Full droplet area (magnification 65X) from procedural blank (a) and drinking water bottles opened/closed 1, 10, and 50 times (b–d). (e–h) High-resolution SEM images of the particulate aggregated at the centre of the droplet footprints in a–d, respectively, magnification 16000X.

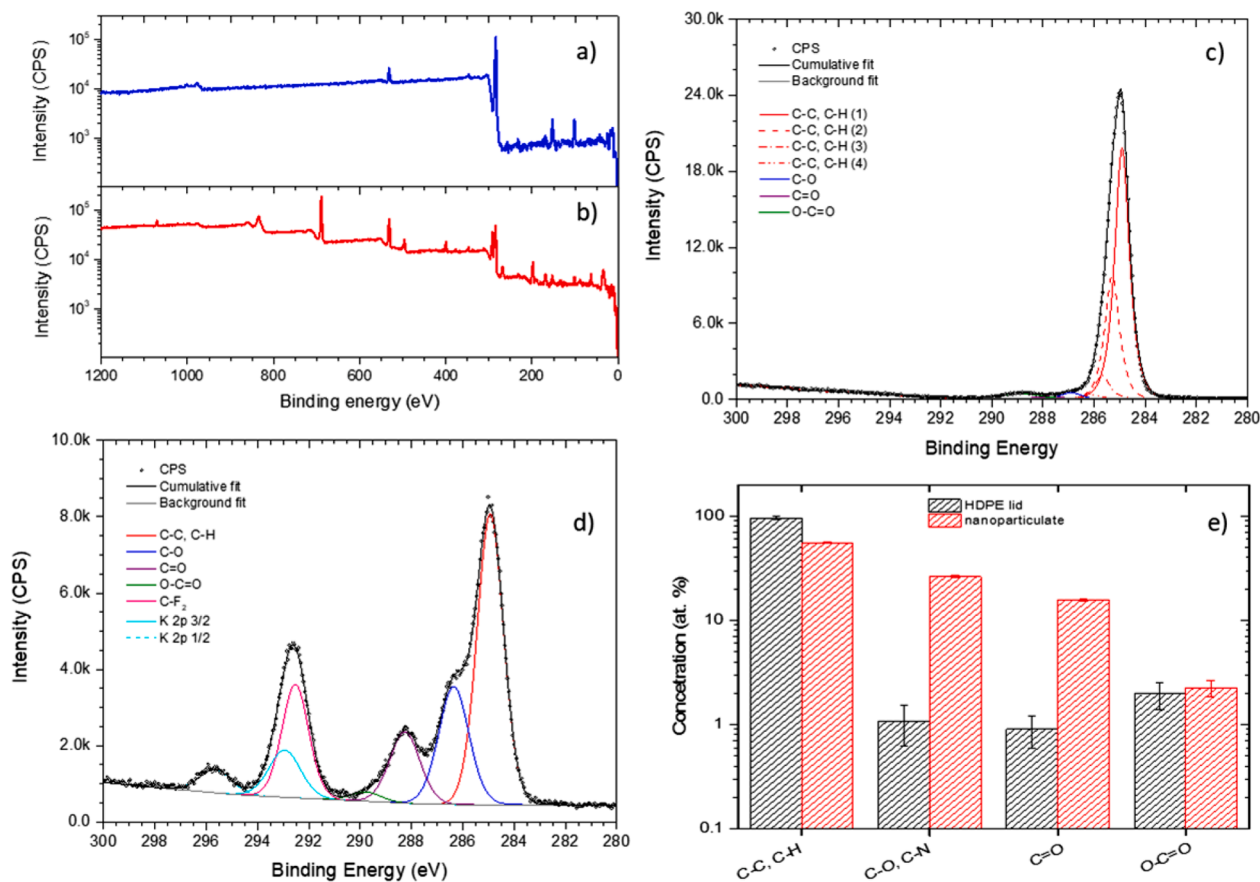


**Fig. 2.** Chemical analysis of the released nanoparticulate surface. XPS survey spectra of (a) the HDPE cap surface (cleaved bulk material) and (b) the concentrated particulate recovered from bottleneck immersion in mQ-H<sub>2</sub>O (50 opening/closing cycles). Concentrated particulates were drop-cast and dried onto clean Teflon substrates. (c) High-resolution C 1s spectra of the HDPE cap surface and associated individual peak contributions fitting (line shapes used are GL(80) for the C-H vibrational components (Beaman et al., 1991) and GL(30) for the oxidized peaks). (d) High-resolution C 1s spectra of the concentrated particulate recovered from bottleneck immersion in mQ-H<sub>2</sub>O (50 opening/closing cycles) (line shapes used are GL(30) for all peaks). (e) Quantification of carbon atom bonds from the deconvolution of the high-resolution C 1s peak envelope for both HDPE cap surface and recovered nanoparticulate (contributions from [CF<sub>2</sub>]<sub>n</sub> substrate was subtracted). Values are also reported in Table S2.

### 3.2. Quantification and sizing

We analysed particle dispersions with Single Particle Extinction and Scattering (SPES) (Potenza et al., 2015). A detailed description of the technique and an explanation of how to interpret data is given in the SI. The four panels in Fig. 3 show SPES histograms for the procedural blank, consisting of mQ-H<sub>2</sub>O undergoing the same manipulations as the bottle samples (Fig. 3a), and the particle dispersions recovered after 1, 10, and 50 (Fig. 3b–d) opening/closing cycles. SPES data for unprocessed mQ-H<sub>2</sub>O are shown in Fig. S8. The scattering data-points cluster in two slightly separated areas which can be qualitatively separated into two distinct particle populations (green and blue circles in Fig. 3c) with different size-distribution characteristics and different behaviour with respect to number of opening/closing cycles. The first group (Population-A), characterised by a high particle concentration, exhibits objects with typically sub-micron dimensions ( $\bar{d}_A = [0.72 \pm 0.09] \mu\text{m}$  with  $d_{FWHM,A} = [0.57 \pm 0.05] \mu\text{m}$ ,  $D_{90,A} = [1.04 \pm 0.14] \mu\text{m}$ ) and refractive index around  $n_A = [1.42 \pm 0.01]$ . All size-distribution descriptors show little variance with the number of opening/closing cycles. In contrast, the second group of particles (Population-B), was present at lower concentrations with typical dimensions being in the low micron range ( $\bar{d}_B = [2.13 \pm 0.50] \mu\text{m}$  with  $d_{FWHM,B} = [1.90 \pm 0.46] \mu\text{m}$ ,  $D_{10,B} = [1.19 \pm 0.32] \mu\text{m}$ ) and  $n_B = [1.41 \pm 0.04]$ . In this case, all descriptors show

higher variance with increasing cycle number. The increasing integral counts of SPES histograms indicates that the total particle concentration in the suspensions also increases with the number of opening/closing cycles, as observed in the SEM pictures. However, the numbers of recovered particles and its dependence on the number of cycles are different when considered separately for the two particle populations (see Fig. S8). Particle counts in Population-A,  $[N]_A$ , is at least an order of magnitude higher than in Population B,  $[N]_B$ , for all the experiments. Another significant difference is that the total number of recovered particles increased roughly linearly ( $r_{\text{Pearson}} = 0.98$ ;  $R_{\text{Adj.}}^2 = 0.94$ ) with the number of cycles for Population-A while it exhibits a plateau for Population-B (see Fig. S9). This would suggest that the former could be linked to the opening-closing cycles while the latter may derive from environmental contamination occurring during manipulation. SPES analysis (Fig. S9) of mQ-H<sub>2</sub>O used for particle recovery reveals that an exceedingly small number of particles with sizes in the low micron range is already present at this stage. A summary with the principal statistical descriptors characterising Population-A number-based particle size distribution is given in Table 1 for different opening-closing cycles and for the control experiments. The full table with all the statistical descriptors of both Population-A and Population-B particle distributions can be found in Table S3 in the Supporting Information section. The overall particle number-based distributions (absolute) as a function of the cycle number and their cumulative distributions (normalised) are

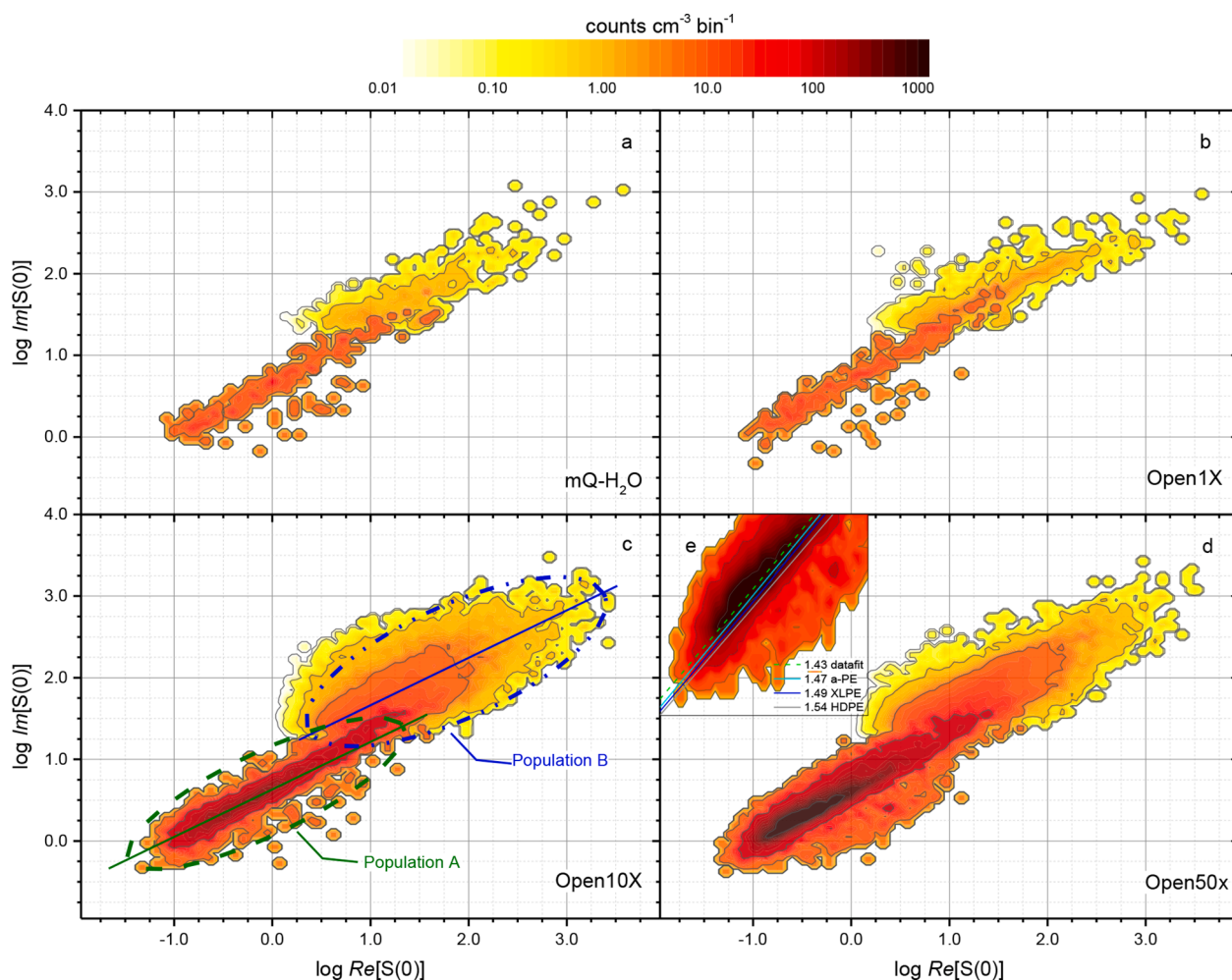


**Fig. 3.** SPES analysis of the released nanoparticulate. Experimental SPES results obtained from (a) procedural blank and suspensions obtained from washing bottlenecks opened 1, 10, and 50 times (b, c and d, respectively). (e) Effective refractive index derived from SPES data of samples compared with expected values from different forms of PE (amorphous PE, XLPE and HDPE). Two-dimensional (2D) plots (histograms) provide the raw data distribution of single particle scattered light fields amplitude in the complex plane  $Re[S(0)]-Im[S(0)]$ . Typically, the scattered field values depend on size, refractive index and shape of each particle.

**Table 1**

Particle size-distributions descriptors from SPES data fitting of Population-A nanoparticles. Absolute number of recovered particles [N] (ad.), refractive index,  $n$  (ad.), distribution mean,  $\bar{d}$  ( $\mu\text{m}$ ). When appropriate, standard deviations are indicated in parentheses. For [N] the relative error in total number of particle estimation is around 20%.

Population A	[N] <sub>A</sub> ad.	$n_A$ ad.	$\bar{d}_A$ $\mu\text{m}$
mQ-H <sub>2</sub> O	1.0E3	– <sup>(c)</sup>	– <sup>(c)</sup>
BLANK	11.8E4	1.43(0.04)	0.75
OPEN 1X	12.4E4	1.41(0.03)	0.82
OPEN 10X	13.5E5	1.43(0.04)	0.69
OPEN 50X	33.0E5	1.43(0.04)	0.64
Average <sup>(a)</sup>	n.a. <sup>(b)</sup>	1.42	0.72
St.Dev. <sup>(a)</sup>	n.a. <sup>(b)</sup>	0.01	0.09

<sup>a</sup> Averages and standard deviations calculated only on OPEN 1x, 10x and 50x

<sup>b</sup> Not applicable.

shown in Fig. 4. An effect caused by the eventual release of MP/NP through the detachment of the security ring from the cap during the first opening of the bottle was not observed. Moreover, the reported numbers of released NP refer to those on the bottleneck, while it can be assumed that further NP remained on the inner surface of caps as reported by Winkler et al. (2019) for MPs/NPs in the size range of 0.54 to 39.9  $\mu\text{m}$ .

To identify the likely source of the released particulate, the refractive index derived from SPES data was compared with HDPE and PET reference values. The best-fit between particle representative data-points belonging to Population-A and Mie scattering calculations (i.e., with constant- $n$  contour lines in the  $[Re[S(O)], Im[S(O)]]$  plane under the assumption of spherical shape) results in an average  $n_A = [1.42 \pm 0.01]$  (inset, Fig. 3e). This value does not substantially vary with the number of cycles. The measured  $n$  value lies in a range compatible with polymeric materials, but it is considerably smaller than the nominal values of the bottle components, PET ( $n_{PET} = 1.57$ ) and HDPE ( $n_{HDPE} = 1.54$ ). Under the working hypothesis that particles observed in Population-A originate mechanically during the opening/closing cycles from the bottleneck-cap system, we can identify at least three factors that may contribute to explaining the difference between observed and calculated refractive indices:

- (i) occurrence of non-isometric nanoparticles, whose  $n_{effective}$  is lower than  $n_{bulk}$ ;
- (ii) occurrence of nanoparticle aggregates, whose  $n_{effective}$  is the volume-average between  $n_{bulk}$  and  $n_{medium}$ ;

- (iii) phase variations occurring during nanoparticle formation during the opening/closing cycles (typically  $n_{amorphous} < n_{crystalline}$ , see Fig. 3e).

As for hypothesis (i), it is often observed that the spherical-shape assumption is rarely met in environmental and/or non-model samples. The occurrence of complex shapes in particulate distribution has the effect of lowering the  $n_{effective}$  value calculated from SPES data (Potenza et al., 2016). Assuming quasi-spherical, non-isometric particles with aspect-ratio  $< 3$  (as can be hypothesised based on SEM images, Fig. S10), the predicted  $n_{effective}$  values (Chyacutelek et al., 1976) would result in  $n_{effective,PE} > 1.46$  and  $n_{effective,PET} > 1.49$ . Support for hypothesis (ii) also derives from SEM analysis (Fig. S10), where the granular appearance of the filtered particulate suggests that they may be composed of smaller sub-units. An analysis of the filling-factor ( $ff$ ) can be made based on the mean-field approximation and the Lorentz-Mie method (Chýlek et al., 1988), assuming the empty volume of the particles is filled with the suspension medium ( $n_{H_2O} = 1.33$ ). To explain the experimentally observed  $n_A$ , particle conglomerates should have  $ff_{PE} = [48.5 \pm 19.1] \%$  and  $ff_{PET} = [42.6 \pm 16.8] \%$ , respectively. These calculations can be qualitatively compared to experimental data using theoretical  $ff$  values predicted for (relatively) monodisperse, randomly packed, isometric hard objects. Depending on the packing mechanism, a theoretical limiting  $ff$  ranging from 52% to 62% can be obtained. A slightly higher  $ff$  could be reached if an external energy source aids conglomerate formation (Nava et al., 2018, 2017). Comparing these theoretical values with the experiments, we can conclude that the conglomerate's scenario is more likely to match the case of PE release. Hypothesis (iii) is made based on the observed amorphization of semicrystalline polymers during mechanical fragmentation (Katiyar et al., 2020). Optical properties of semicrystalline polymers are related to their structural characteristics, such as crystalline fraction ( $X_c$ ), and the refractive index of crystalline domains is normally higher than that of amorphous regions according to their relative densities. Commercial PET presents  $X_c$  around 20–30% (determined by calorimetry (Bach et al., 2009a)) and  $n_{PET} = 1.57$ ; while in the HDPE bottle caps, an  $X_c = 80\%$  was determined by X-ray diffraction (XRD) measurements (Nava et al., 2017) (Fig. S11) and  $n_{HDPE} = 1.54$ . The refractive index of purely amorphous PET has been measured to be around  $n_{amorph-PET} = 1.54$ ; (Iiyama et al., 2011) while in different PE formulations the correlation between  $X_c$  and  $n$  is clear, e.g.,  $n_{LDPE} = 1.51$ ,  $X_{c,LDPE} \approx 50\%$ ;  $n_{XLPE} = 1.49$ ,  $X_{c,XLPE} \approx 40\%$  and  $n_{amorph-PE} = 1.47$ ,  $X_{c,amorph-PE} \approx 0\%$ . Some of these values have been used to calculate the constant- $n$  lines in Fig. 3e and compared to the data best-fit

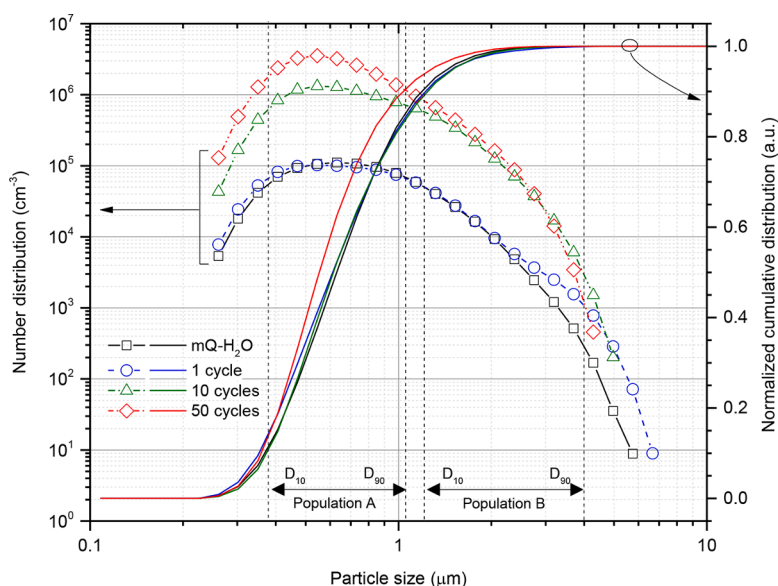


**Fig. 4.** Quantitative description of the released nanoparticulate. Number-based particle size distribution (left axis) and normalised cumulative particle size distribution obtained from SPES experiments with mQ-H<sub>2</sub>O (procedural blank) and suspensions obtained from washing bottlenecks opened 1, 10, and 50 times. Dotted lines indicated the boundaries of Population-A and B particle distributions expressed in terms  $D_{10}$  and  $D_{90}$  as calculated from SPES histograms. The average volume analysed per sample was  $V = [15 \pm 0.3] \text{ mL}$ .

line for Population-A. The trend in particle concentrations and the three scenarios proposed in the previous paragraph are qualitatively consistent with the hypothesis that particulates in Population-A originate from the PE cap system under the influence of the opening/closing cycles. Nonetheless, none of these effects alone can be invoked to unambiguously explain the discrepancy between the observed  $n_A$  value and  $n_{PE}$ , and univocal identification of the chemical nature of the nanoparticles based only on these observations is not possible.

### 3.3. Chemical identification

To unequivocally identify the particle's chemical nature, we further analysed the particulate residue via  $\mu$ -Raman spectroscopy. Fig. 5a shows spectra in the group frequencies and characteristic  $CH_2$ -stretching regions measured on the nanoparticulate recovered after 1, 10, and 50 cycles. Particulate spectra are compared to the HDPE cap spectrum and literature (Bentley and Hendra, 1995; Gaston et al., 2018; Snyder et al., 1978; Zhang et al., 1997) (Fig. S12). Fig. 5b–e shows surface maps displaying integrated Raman intensity in the spectral range between 1400 and 1500  $cm^{-1}$ , a region characteristic of functional group vibrations  $\delta(CH_2)$  and  $\delta(CH_3)$  and compatible with both natural organic materials and carbon-based polymeric materials. Both single-point Raman spectra and intensity maps support the SEM and SPES observations which indicate that the recovered particles in the submicron-size range increase in number with the number of opening/closing cycles and can be distinguished from those of procedural blanks. Particulate chemical identification based on standard automated spectral correlation operated using different commercial and home-built reference material libraries (Cowger et al., 2021) did not show any reliable match with either the packaging materials (HDPE, PET), expected impurities (based on XPS analysis) or known contaminants from our preparation protocol. In general, spectra from recovered particulates show a marked intensity loss, high signal-to-noise ( $S/N$ ) ratio and poorly defined, broad spectral features compared to the bulk material. This is due to reduced scattering material volume in the laser focal spot, reduced particle size, and inhomogeneous broadening effects (mainly due to morphological inhomogeneity in our sample). The Raman bands with the highest  $S/N$

were recorded for the 50 cycles sample, exhibiting also the highest particulate concentration. Raman bands from the samples appear in similar spectral regions where the HDPE cap also exhibits Raman bands, however, band head positions and individual peak shapes appear to be different between the bulk and the nanomaterials.

To gain insight into the chemical nature of the recovered nanoparticle, we closely analysed the group frequencies region (1000–1550  $cm^{-1}$ , Fig. 6a, b) and the  $\nu(CH_2)$  region (2775–3025  $cm^{-1}$ , Fig. 6d–f). The features of the spectra from recovered particulates (Fig. 6a) were compared with model nanoparticulate obtained by cryomilling HDPE bottle caps (after resuspension in mQ-H<sub>2</sub>O and filtration with a 1.2  $\mu m$  cut-off filter, Fig. 6b) and the HDPE cap spectra (Fig. 6c). The cryomilled material was included to separate possible thermal effects in NP formation occurring during cycling. Raman band assignments for semi-crystalline PE molecular vibrations are well established in the literature; (Bentley and Hendra, 1995; Gaston et al., 2018; Snyder et al., 1978; Zhang et al., 1997) Table S4 summarises the Raman shifts, vibrational modes and structural phase assignments for all the individual peaks obtained from band envelopes deconvolution shown in Fig. 6. In Fig. 6, the different peak phase assignments are colour-coded for ease of reference; orange is assigned to the orthorhombic crystalline phase, green for all non-crystalline consecutive *trans* (NCCT) (Migler et al., 2015) configurations and blue for amorphous domains. All peaks identified in the HDPE spectrum were identified and phase-assigned, (Bentley and Hendra, 1995; Gaston et al., 2018; Snyder et al., 1978; Zhang et al., 1997) and the resulting crystallinity calculated (Rull et al., 1993) from experiments was found to be as follows:  $X_{orthorhombic\_Raman} = [10.3 \pm 0.5] \%$ ,  $(X_{amorph\_Raman} = [18.3 \pm 0.5] \%)$  and  $X_{NCCT\_Raman} = [71.4 \pm 0.5] \%$ . This result agrees with the XRD measurements (see Fig. S11, which give a compound crystalline fraction of  $X_{orthorhombic+NCCT\_XRD} = [78.9 \pm 0.5] \%$  and an amorphous fraction of  $X_{amorph\_XRD} = [21.1 \pm 0.5] \%$  in agreement also with reference values for commercial HDPE (Bach et al., 2009b) For the two nanomaterials, the first band in the group frequencies region (Fig. 6a, b) shows two peaks degrading towards higher wavenumbers and extends from 1000 to 1150  $cm^{-1}$ . The second band is a broad, featureless peak centred around 1300  $cm^{-1}$ , while the third band shows two components of increasing intensity and extends

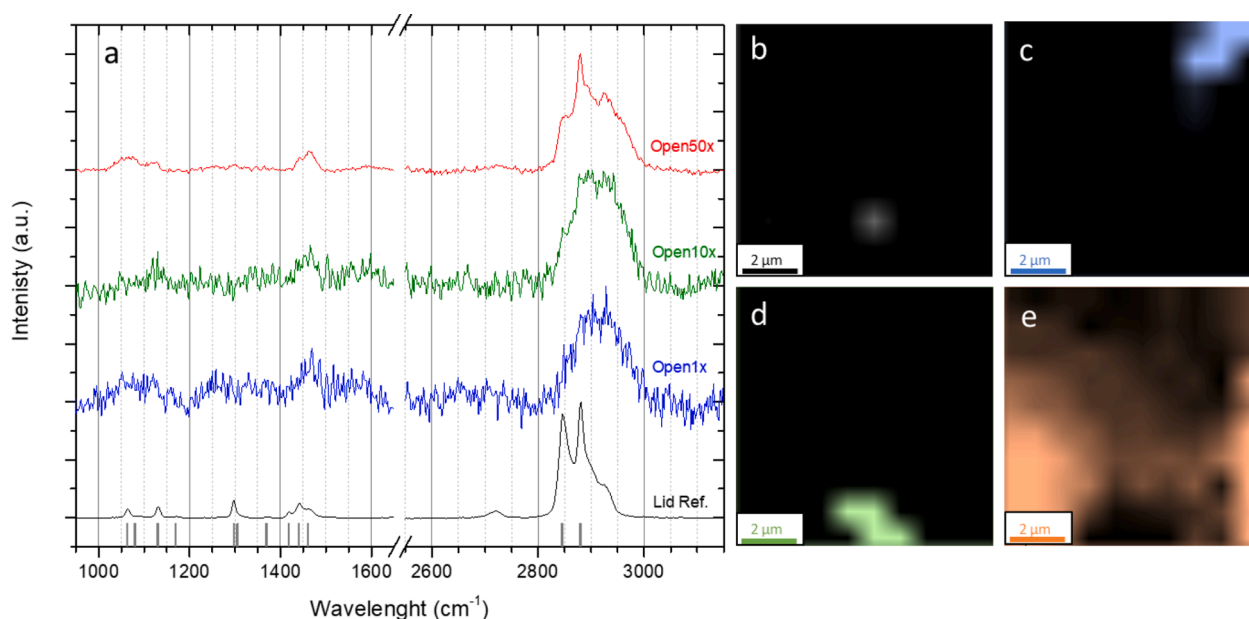


**Fig. 5.** Chemical analysis of the released nanoparticulate. (a) Confocal Raman spectrum of the water bottle HDPE cap surface (black) and particulate recovered from water bottle opened/closed 1 (blue), 10 (green), and 50 (red) times. Data are shown in the group frequencies and  $CH_2$ -stretching distinct regions. Black vertical lines above the X-axis represent HDPE reference Raman peak centre positions taken from literature (Bentley and Hendra, 1995; Gaston et al., 2018; Snyder et al., 1978; Zhang et al., 1997). (b–e) Univariate Raman maps of the selected sample area (rim of the droplet) from concentrated samples of procedural blanks and bottles opened/closed for 1, 10, and 50 cycles. The maps were generated by plotting integrated intensity in the spectral range at 1400–1500  $cm^{-1}$ .

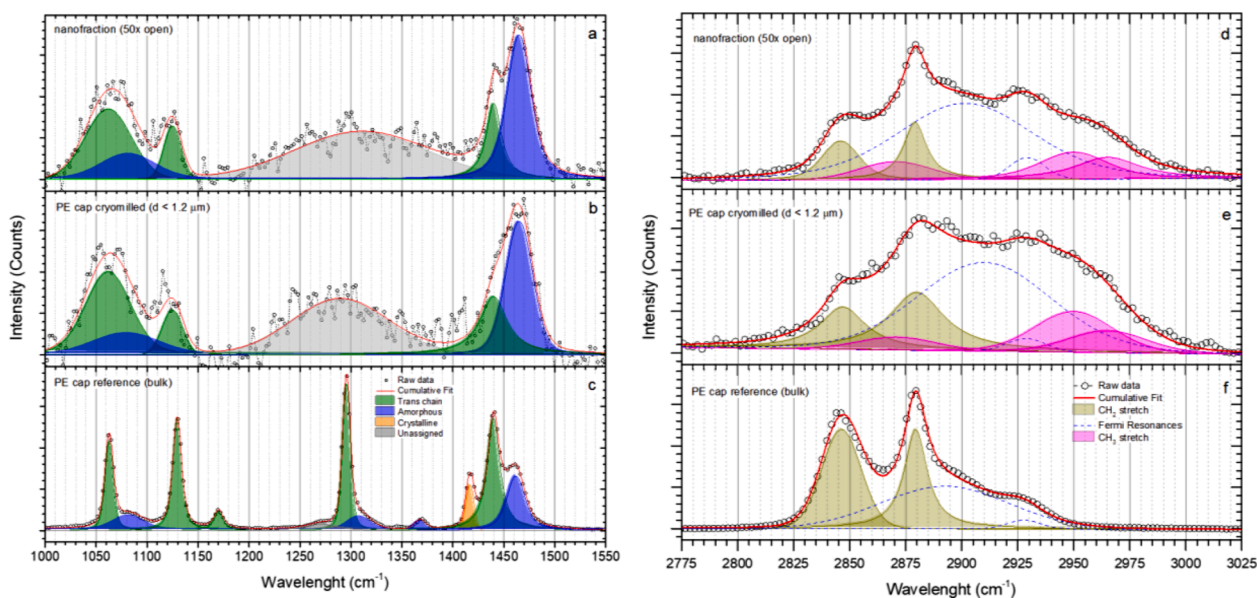


**Fig. 6.** Chemical identification of the released nanoparticulate. Raman spectra and spectral features deconvolution in the 1000–1550  $\text{cm}^{-1}$  group frequencies region for (a) the particulate recovered from washing the bottleneck (50 cycles), (b) for the filtered fraction from cryomilled PE cap material, and (c) PE cap bulk reference. Data are normalised to maximum intensity. Raman spectra and spectral features deconvolution in the 2775–3025  $\text{cm}^{-1}$   $\text{CH}_x$  stretch frequencies region for (d) the material recovered from cap washing opened 50 times, (e) the filtered fraction from cryomilled PE cap, and (f) the PE cap bulk material reference. Data are normalised to maximum intensity.

from 1400 to 1500  $\text{cm}^{-1}$ . The fourth band (Fig. 6d, e) is located at higher wavenumbers and extends from 2800 to 3000  $\text{cm}^{-1}$ , showing several poorly resolved band heads. In literature, the fundamental Raman bands occurring in these regions have been confidently assigned to  $\nu(\text{C-C})$  from aliphatic chains,  $\tau(\text{CH}_2)$  and  $\delta(\text{CH}_2)$ , respectively, for PE and several other polyolefins (Corsetti et al., 2017; Furukawa et al., 2006; Snyder et al., 1978; Tomba et al., 2019). Knowing the assignment of HDPE cap spectral features allows a detailed comparison with the spectra of both types of nanoparticulate. We note that the spectral features in Fig. 6a, b can be confidently reconstructed using a subgroup of HDPE individual peaks keeping their Raman-shift fixed (but varying intensity and FWHM). The peaks observed in the nanoparticulate spectra belong either to the amorphous or *trans* conformations but not to the crystalline orthorhombic phase. In general, the following observations hold:

- (i) Raman-shifts for different peaks do not vary in all three analysed materials. FWHM increases in all nanomaterials with respect to bulk HDPE.
- (ii) Nanoparticulate show decreased relative intensities of  $\nu(\text{C-C})$  and  $\delta(\text{CH}_2)$  Raman bands components assigned to *trans* configurations.
- (iii) Nanoparticulate show increased relative intensities in the same spectral regions for peaks assigned to amorphous conformational components.
- (iv) Nanoparticulate show a decrease and broadening of the whole  $\tau(\text{CH}_2)$  band.
- (v) The peak related to the orthorhombic crystalline phase (at 1416  $\text{cm}^{-1}$ ) is absent in the nanoparticulate.

Moreover, the spectrum of the recovered nanoparticulate qualitatively resembles spectra recorded for melt phase HDPE obtained during high temperature recrystallisation (Jin et al., 2017). Crystallinity evaluated from the two nanomaterial Raman spectra is zero due to the absence of the 1416  $\text{cm}^{-1}$  peak, but control measurements via XRD were not possible due to the low amount of the recovered nanoparticulate and the cryomilled nanofraction remaining after filtration with the 1.2  $\mu\text{m}$  cut-off filters. However, spectra taken on the unfractionated cryomilled particulates (without filtration steps, with a broad size distribution

spanning up to several tens of  $\mu\text{m}$ ) reveal a 40% increase of the amorphous PE fraction (see Fig. S11). Raman results are consistent with the observed reduction in the measured refractive index for Population-A in the SPES histograms (Fig. 2e), thus supporting a scenario in which nanoparticles are produced by mechanical action during opening/closing cycles and originate from the HDPE cap. These secondary nanomaterials may degrade and lose their crystalline character during formation, resulting in amorphous PE nanoparticles. The PE assignment of the unknown nanoparticulate, according to  $\mu$ -Raman analysis, implying their origin from the bottle screw cap and not from the PET-made bottleneck is also supported by comparing Raman, FTIR and EDX spectra of the recovered particulate with the corresponding reference spectra for the bulk materials shown in Figs. S1, S3–S7, and 2c. The  $\nu(\text{CH}_x)$  region (2800–3000  $\text{cm}^{-1}$ ) for the same three materials is treated separately (Fig. 6d–f) as it provides a different kind of information. The reference HDPE cap spectrum exhibits the common band structure for this material (Bentley and Hendra, 1995; Howell et al., 1999; Snyder et al., 1978; Zhang et al., 1997). The two narrow band heads can be assigned to the  $\nu_s(\text{CH}_2)$  (2845  $\text{cm}^{-1}$ ) and  $\nu_{as}(\text{CH}_2)$  (2880  $\text{cm}^{-1}$ ) modes. They contain contributions from amorphous and crystalline regions and have no definite phase assignment. The broad spectral features forming the high-wavenumber band tail arise due to Fermi resonances between the  $\nu_s(\text{CH}_2)$  vibration at 2845  $\text{cm}^{-1}$  and the  $\delta(\text{CH}_2)$  at 1440  $\text{cm}^{-1}$  (Snyder et al., 1978). These broad features carry most of the integrated band intensity, and their predicted Raman shifts are around 2900 and 2930  $\text{cm}^{-1}$  (Snyder et al., 1978). These contributions should not be confused with  $\nu_{as}(\text{CH}_3)$  vibrations located at slightly higher wavenumbers (2952 and 2964  $\text{cm}^{-1}$ ). Highly crystalline HDPE is normally characterized by long, linear hydrocarbon chains exhibiting high molecular weight and low branching (< 1%) resulting in an extremely low  $\text{CH}_3/\text{CH}_2$  ratio, so methyl-terminations contributions are normally negligible for this polymer. Spectral analysis for the nanoparticulate reveals how typical PE  $\nu(\text{CH}_2)$  vibrations band structure is also preserved in the two nanomaterials. Both  $\nu_s(\text{CH}_2)$  and  $\nu_{as}(\text{CH}_2)$  individual peaks are detected at the expected Raman-shift (Bentley and Hendra, 1995), even though they appear broader and less intense. We also observe that their intensity ratio ( $I_{2845}/I_{2880}$ ) is slightly decreased. However, interpretation is not straightforward due to the relative

uncertainty introduced by evaluating the contribution of the broad underlying Fermi resonance bands (Snyder et al., 1978; Zhang et al., 1997). A marked difference between bulk and nanomaterials spectra is the appearance of an intense band tail at high wavenumbers with non-negligible intensity in the region 2930–2980  $\text{cm}^{-1}$ . Raman intensity in this spectral region is normally not observed in common PE-based materials (e.g., HDPE [this study], LDPE (Portesi et al., 2019) or XLPE (Fig. S13), irrespective of their crystallinity degree and cross-linking. This band is fitted with two additional peaks (Fig. 6d, e) centred at 2852 and 2964  $\text{cm}^{-1}$ . Moreover, an additional component (2871  $\text{cm}^{-1}$ ) is observed between the two  $\nu(\text{CH}_2)$  peaks. The observed Raman-shifts of these peaks match with the predicted shifts and relative intensities of methyl- terminations stretching modes in aliphatic chains (Snyder et al., 1978). More precisely, the assignments are  $\nu_s(\text{CH}_3)$  (2871  $\text{cm}^{-1}$ ), in-plane  $\nu_{as}(\text{CH}_3)$  (2852  $\text{cm}^{-1}$ ) and its out-of-plane counterpart (2964  $\text{cm}^{-1}$ ). These peaks indicate a marked increase in the number density of methyl terminations in the nanoparticulate sample compared to the cap material and could suggest the occurrence of PE linear chains scission events (Veitmann et al., 2014) induced by mechanical stresses acting during nanoparticle formation upon cycling. Not surprisingly, the nanomaterials  $\nu(\text{CH}_x)$  band appearance is qualitatively similar to the spectral shape of the same region measured in short-chained polyolefins in the liquid state (Tomba et al., 2019). The similarity between the recovered nanoparticles spectra and the cryomilled sample supports the hypothesis that the main mechanisms responsible for nanoparticle formation and amorphization have a mechanical origin.

#### 4. Conclusion

In conclusion, NP release from drinking water plastic bottles under simulated use was observed and characterised combining SEM, XPS, SPES and  $\mu$ -Raman analysis. The combination of SPES and  $\mu$ -Raman represent the minimal set of techniques necessary to apply the methodology for the quantification and identification of NP in simple matrices like drinking water. The size distribution of nanoparticles released from the packaging ranged from  $D_{10,A} = [0.38 \pm 0.03] \mu\text{m}$  to  $D_{90,A} = [1.04 \pm 0.14] \mu\text{m}$ , possibly extending to lower sizes below the SPES detection limit (200 nm). Nanoparticles were composed of amorphous PE, likely originating from HDPE caps via mechanical action during opening/closing cycles. From the SPES size distribution data and considering particle shape and fill-factor approximations, the total mass of amorphous PE in the form of nanoparticles released can be estimated not to exceed a few tenths of ng per cycle. This study shows that, in a realistic environment, stressors acting during the top-down formation of NPs may alter the physical-chemical characteristics of the nanoparticulate with respect to those of their original source bulk material, thus hindering their identification. We have found out that even mechanical stress alone acting during NP formation can degrade the materials even without the occurrence of other external stressors. Analytical detection methods development, understanding the physical-chemical processes occurring during secondary generation and the design of relevant NP models can be linked in a circular positive feedback loop. We have shown that the design of improved analytical schemes for secondary NP identification and quantification allows for further insights into material degradation/fragmentation processes. A deeper understanding of degradation mechanisms during secondary NP formation could then be used to design improved model NP materials that could be exploited for further developing analytical methods. Moreover, the effect of degradation/fragmentation pathways on physical-chemical properties of the NP should also be taken into account during the design of model engineered nanomaterials for use in studies about secondary NP fate, effects on human health, sampling and analysis (Gigault et al., 2021).

#### Author contributions

The manuscript was written through contributions of all authors. All authors have given approval to the final version of the manuscript. These authors contributed equally: Anna Winkler, Francesco Fumagalli. AW, CC and AV designed the study and prepared the samples. CC prepared and executed SPES experiments. AV executed Raman measurements. AV and AW executed SEM analysis. FF performed FTIR and XPS measurements; he also analyzed, and interpreted SPES, Raman and XPS data. DG and PT supervised the overall work and contributed to the results discussion/manuscript drafting.

#### Funding sources

This research was conducted under the framework of the JRC Research Infrastructure Access Agreement No. 335559/11 2019-1-RD-Nanobiotech, "Open access to JRC Research Infrastructures." under the supervision of Dr. Pascal Colpo (EU-JRC Ispra, Unit F.2).

#### Declaration of Competing Interest

None.

#### Data availability

Data will be made available on request.

#### Acknowledgments

The authors acknowledge Dr. Giacomo Ceccone (EU-JRC Ispra, Unit F.2) for valuable discussions and technical help with XPS data fitting. Dr. Tiziano Sanvito (EOS S.r.l., Milano, Italy) is acknowledged for the fruitful discussion about SPES data interpretation.

#### Supplementary materials

Supplementary material associated with this article can be found, in the online version, at doi:10.1016/j.watres.2022.118848.

#### References

- Allan, J., Belz, S., Hoeveler, A., Hugas, M., Okuda, H., Patri, A., Rauscher, H., Silva, P., Slikker, W., B., S.K., Tong, W., Anklam, E., 2021. Regulatory landscape of nanotechnology and nanoplastics from a global perspective. *Regul. Toxicol. Pharmacol.* 122 <https://doi.org/10.1016/j.yrtph.2021.104885>.
- Bach, C., Dauchy, X., Etienne, S., 2009a. Characterization of poly(ethylene terephthalate) used in commercial bottled water. *IOP Conf. Ser. Mater. Sci. Eng.* <https://doi.org/10.1088/1757-899X/5/1/012005>.
- Bach, C., Dauchy, X., Etienne, S., 2009b. Characterization of poly(ethylene terephthalate) used in commercial bottled water. *IOP Conf. Ser. Mater. Sci. Eng.* 5 <https://doi.org/10.1088/1757-899X/5/1/012005>.
- Baer, D.R., Engelhard, M.H., 2010. XPS analysis of nanostructured materials and biological surfaces. *J. Electron Spectrosc. Relat. Phenom.* 178–179, 415–432. <https://doi.org/10.1016/j.elspec.2009.09.003>.
- Bañuls-Ciscar, J., Fumagalli, F., Ruiz-Moreno, A., Rossi, F., Suraci, S.V., Fabiani, D., Ceccone, G., 2020. A methodology to investigate heterogeneous oxidation of thermally aged cross-linked polyethylene by ToF-SIMS. *Surf. Interface Anal.* 52, 1178–1184. <https://doi.org/10.1002/sia.6848>.
- Beamson, G., Clark, D.T., Kendrick, J., Briggs, D., 1991. Observation of vibrational asymmetry in the high resolution monochromatized XPS of hydrocarbon polymers.
- Bennet, F., Müller, A., Radnik, J., Hachenberger, Y., Jungnickel, H., Laux, P., Luch, A., Tentschert, J., 2020. Preparation of nanoparticles for ToF-SIMS and XPS analysis. *J. Vis. Exp.* 163.
- Bentley, P.A., Hendra, P.J., 1995. Polarised FT Raman studies of an ultra-high modulus polyethylene rod. *Spectrochim. Acta Part A Mol. Biomol. Spectrosc.* 51, 2125–2131. [https://doi.org/10.1016/0584-8539\(95\)01513-3](https://doi.org/10.1016/0584-8539(95)01513-3).
- Blanco, F., Davranche, M., Fumagalli, F., Ceccone, G., Gigault, J., 2021. A reliable procedure to obtain environmentally relevant nanoplastic proxies. *Environ. Sci. Nano* 8, 3211–3219. <https://doi.org/10.1039/D1EN00395J>.
- Bohren, C.F., Huffman, D.R., 1998. Absorption and scattering of light by small particles. *Absorption and Scattering of Light by Small Particles.* <https://doi.org/10.1002/9783527618156>.

- Cella, C., La Spina, R., Mehn, D., Fumagalli, F., Ceccone, G., Valsesia, A., Gilliland, D., 2022. Detecting micro- and nanoplastics released from food packaging: challenges and analytical strategies. *Polymers*. <https://doi.org/10.3390/polym14061238>.
- Chyacutelek, P., Grams, G.W., Pinnick, R.G., 1976. Light scattering by irregular randomly oriented particles. *Science* 193, 480–482. <https://doi.org/10.1126/SCIENCE.193.4252.480>.
- Chýlek, P., Wang, R.T., Pinnick, R.G., Srivastava, V., 1988. Scattering of electromagnetic waves by composite spherical particles: experiment and effective medium approximations. *Appl. Opt.* 27 (12), 2396–2404. <https://doi.org/10.1364/AO.27.002396>, pp. 2396–2404 27.
- Corsetti, S., Rabl, T., McGloin, D., Kiefer, J., 2017. Intermediate phases during solid to liquid transitions in long-chain n-alkanes. *Phys. Chem. Chem. Phys.* 19, 13941–13950. <https://doi.org/10.1039/C7CP01468F>.
- Cowger, W., Steinmetz, Z., Gray, A., Munno, K., Lynch, J., Hapich, H., Primpke, S., Frond, H.De, Rochman, C., Herodotou, O., 2021. Microplastic spectral classification needs an open source community: open specy to the rescue! *Anal. Chem.* 93, 7543–7548. <https://doi.org/10.1021/ACS.ANALCHEM.1C00123>.
- Cox, K.D., Covernton, G.A., Davies, H.L., Dower, J.F., Juanes, F., Dudas, S.E., 2019. Human consumption of microplastics. *Environ. Sci. Technol.* 53, 7068–7074. <https://doi.org/10.1021/ACS.EST.9B01517>.
- Du, F., Cai, H., Zhang, Q., Chen, Q., Shi, H., 2020. Microplastics in take-out food containers. *J. Hazard. Mater.* 399, 122969 <https://doi.org/10.1016/J.JHAZMAT.2020.122969>.
- Facchetti, S.V., La Spina, R., Fumagalli, F., Riccardi, N., Gilliland, D., Ponti, J., 2020. Detection of metal-doped fluorescent PVC microplastics in freshwater mussels. *Nanomaterials* 10, 1–14. <https://doi.org/10.3390/nano10122363>.
- Fadare, O.O., Wan, B., Guo, L.H., Zhao, L., 2020. Microplastics from consumer plastic food containers: are we consuming it? *Chemosphere* 253, 126787. <https://doi.org/10.1016/J.CHEMOSPHERE.2020.126787>.
- Furukawa, T., Sato, H., Kita, Y., Matsukawa, K., Yamaguchi, H., Ochiai, S., Siesler, H.W., Ozaki, Y., 2006. Molecular structure, crystallinity and morphology of polyethylene/polypropylene blends studied by Raman mapping, scanning electron microscopy, wide angle X-ray diffraction, and differential scanning calorimetry. *Polym. J.* 38, 1127–1136. <https://doi.org/10.1295/polymj.PJ2006056>.
- Galafassi, S., Di Cesare, A., Di Nardo, L., Sabatino, R., Valsesia, A., Fumagalli, F., G., C., Volta, P., 2021. Microplastic retention in small and medium municipal wastewater treatment plants and the role of the disinfection. *Environ. Sci. Pollut. Res. Int.* <https://doi.org/10.1007/S11356-021-16453-2>.
- Gaston, F., Dupuy, N., Marque, S.R.A., Dorey, S., 2018. Evaluation of multilayer film stability by Raman spectroscopy after gamma-irradiation sterilization process. *Vib. Spectrosc.* 96, 52–59. <https://doi.org/10.1016/J.VIBSPEC.2018.03.002>.
- Gigault, J., El Hadri, H., Nguyen, B., Grassl, B., Rowenczyk, L., Tufenkji, N., Feng, S., Wiesner, M., 2021. Nanoplastics are neither microplastics nor engineered nanoparticles. *Nat. Nanotechnol.* 16, 501–507. <https://doi.org/10.1038/s41565-021-00886-4>.
- Gillibert, R., Balakrishnan, G., Deshoules, Q., Tardivel, M., Magazzù, A., Donato, M.G., Maragò, O.M., Lamy De La Chapelle, M., Colas, F., Lagarde, F., Gucciardi, P.G., 2019. Raman tweezers for small microplastics and nanoplastics identification in seawater. *Environ. Sci. Technol.* 53, 9003–9013. <https://doi.org/10.1021/acs.est.9b03105>.
- Gniadek, M., Dabrowska, A., 2019. The marine nano- and microplastics characterisation by SEM-EDX: the potential of the method in comparison with various physical and chemical approaches. *Mar. Pollut. Bull.* 148, 210–216. <https://doi.org/10.1016/J.MARPOLBUL.2019.07.067>.
- Hamzah, M., Khenfouch, M., Rjeb, A., Sayouri, S., Houssaini, D.S., Darhour, M., Srinivasu, V.V., 2018. Surface chemistry changes and microstructure evaluation of low density nanocluster polyethylene under natural weathering: a spectroscopic investigation. *J. Phys. Conf. Ser.* <https://doi.org/10.1088/1742-6596/984/1/012010>. Institute of Physics Publishing.
- Hernandez, L.M., Xu, E.G., Larsson, H.C.E., Tahara, R., Maisuria, V.B., Tufenkji, N., 2019. Plastic teabags release billions of microplastics and nanoplastics into tea. *Environ. Sci. Technol.* 53, 12300–12310. <https://doi.org/10.1021/acs.est.9b02540>.
- Howell, N.K., Arteaga, G., Nakai, S., Li-Chan, E.C.Y., 1999. Raman spectral analysis in the C-H stretching region of proteins and amino acids for investigation of hydrophobic interactions. *J. Agric. Food Chem.* 47, 924–933. <https://doi.org/10.1021/jf9810741>.
- Iiyama, K., Ishida, T., Ono, Y., Maruyama, T., Yamagishi, T., 2011. Fabrication and characterization of amorphous polyethylene terephthalate optical waveguides. *IEEE Photonics Technol. Lett.* 23, 275–277. <https://doi.org/10.1109/LPT.2010.2101058>.
- Jin, Y., Kotula, A.P., Snyder, C.R., Hight Walker, A.R., Migler, K.B., Lee, Y.J., 2017. Raman identification of multiple melting peaks of polyethylene. *Macromolecules* 50, 6174–6183. <https://doi.org/10.1021/ACS.MACROMOL.7B01055>.
- Katiyar, N.K., Biswas, K., Tiwary, C.S., 2020. Cryomilling as environmentally friendly synthesis route to prepare nanomaterials. 10.1080/09506608.2020.1825175 66, 493–532. 10.1080/09506608.2020.1825175.
- Kedzierski, M., Lechat, B., Sire, O., Le Maguer, G., Le Tilly, V., Bruzaud, S., 2020. Microplastic contamination of packaged meat: occurrence and associated risks. *Food Packag. Shelf Life* 24, 100489. <https://doi.org/10.1016/J.FPSL.2020.100489>.
- Kögel, T., Bjørøy, Ø., Toto, B., Bienfait, A.M., Sanden, M., 2020. Micro- and nanoplastic toxicity on aquatic life: determining factors. *Sci. Total Environ.* 709, 136050 <https://doi.org/10.1016/J.SCI.TOTENV.2019.136050>.
- Laborda, F., Trujillo, C., Lobinski, R., 2021. Analysis of microplastics in consumer products by single particle-inductively coupled plasma mass spectrometry using the carbon-13 isotope. *Talanta* 221, 121486. <https://doi.org/10.1016/J.TALANTA.2020.121486>.
- Lim, X.Z., 2021. Microplastics are everywhere - but are they harmful? *Nature* 593, 22–25. <https://doi.org/10.1038/D41586-021-01143-3>.
- Lin, W., Jiang, R., Hu, S., Xiao, X., Wu, J., Wei, S., Xiong, Y., Ouyang, G., 2019. Investigating the toxicities of different functionalized polystyrene nanoplastics on *Daphnia magna*. *Ecotoxicol. Environ. Saf.* 180, 509–516. <https://doi.org/10.1016/J.ECOENV.2019.05.036>.
- Liu, G., Wang, J., Wang, M., Ying, R., Li, X., Hu, Z., Zhang, Y., 2022. Disposable plastic materials release microplastics and harmful substances in hot water. *Sci. Total Environ.* 818, 151685 <https://doi.org/10.1016/J.SCI.TOTENV.2021.151685>.
- Liu, P., Zhan, X., Wu, X., Li, J., Wang, H., Gao, S., 2020. Effect of weathering on environmental behavior of microplastics: properties, sorption and potential risks. *Chemosphere* 242. <https://doi.org/10.1016/J.CHEMOSPHERE.2019.125193>.
- Materić, D., Kasper-Giebl, A., Kau, D., Anten, M., Greilinger, M., Ludewig, E., Sebillé, E. van, Röckmann, T., Holzinger, R., 2020. Micro- and nanoplastics in alpine snow: a new method for chemical identification and (semi)quantification in the nanogram range. *Environ. Sci. Technol.* 54, 2353–2359. <https://doi.org/10.1021/ACS.EST.9B07540>.
- Migler, K.B., Kotula, A.P., Walker, A.R.H., 2015. Trans-rich structures in early stage crystallization of polyethylene. *Macromolecules* 48, 4555–4561. <https://doi.org/10.1021/MA5025895>.
- Mitrano, D.M., Wick, P., Nowack, B., 2021. Placing nanoplastics in the context of global plastic pollution. *Nat. Nanotechnol.* 16, 491–500. <https://doi.org/10.1038/s41565-021-00888-2>.
- Nava, G., Fumagalli, F., Fonzo, F.Di, 2018. Large area porous 1D photonic crystals comprising silicon hierarchical nanostructures grown by plasma-assisted, nanoparticle jet deposition. *Artic. Nanotechnology* <https://doi.org/10.1088/1361-6528/aade21>.
- Nava, G., Fumagalli, F., Gambino, S., Farella, I., Dell'Erba, G., Beretta, D., Divitini, G., Ducati, C., Caironi, M., Cola, A., Di Fonzo, F., 2017. Towards an electronic grade nanoparticle-assembled silicon thin film by ballistic deposition at room temperature: the deposition method, and structural and electronic properties. *J. Mater. Chem. C* 5. <https://doi.org/10.1039/C7TC00187H>.
- Portesi, C., Visentin, D., Durbiano, F., Abete, M.C., Rizzi, M., Maurino, V., Rossi, A.M., 2019. Development of a rapid micro-Raman spectroscopy approach for detection of NIAS in LDPE pellets and extruded films for food packaging applications. *Polym. Test.* 80, 106098 <https://doi.org/10.1016/J.POLYMERTESTING.2019.106098>.
- Potenza, M.A.C., Albani, S., Delmonte, B., Villa, S., Sanvito, T., Paroli, B., Pullia, A., Baccolo, G., Mahowald, N., Maggi, V., 2016. Shape and size constraints on dust optical properties from the Dome C ice core, Antarctica. *Sci. Rep.* 6 <https://doi.org/10.1038/srep28162>.
- Potenza, M.A.C., Sanvito, T., Argenti, S., Cella, C., Paroli, B., Lenardi, C., Milani, P., 2015. Single particle optical extinction and scattering allows real time quantitative characterization of drug payload and degradation of polymeric nanoparticles. *Sci. Rep.* 5, 1–9. <https://doi.org/10.1038/srep18228>, 2015 51.
- Potenza, M.A.C., Sanvito, T., Pullia, A., 2015. Measuring the complex field scattered by single submicron particles. *AIP Adv.* 5, 117222 <https://doi.org/10.1063/1.4935927>.
- Ranjan, V.P., Joseph, A., Goel, S., 2021. Microplastics and other harmful substances released from disposable paper cups into hot water. *J. Hazard. Mater.* 404, 124118 <https://doi.org/10.1016/J.JHAZMAT.2020.124118>.
- Rull, F., Prieto, A.C., Casado, J.M., Sobron, F., Edwards, H.G.M., 1993. Estimation of crystallinity in polyethylene by Raman spectroscopy. *J. Raman Spectrosc.*
- Sanvito, T., Bigini, P., Cavanna, M.V., Fiordaliso, F., Violatto, M.B., Talamini, L., Salmona, M., Milani, P., Potenza, M.A.C., 2017. Single particle extinction and scattering optical method unveils in real time the influence of the blood components on polymeric nanoparticles. *Nanomed. Nanotechnol. Biol. Med.* 13, 2597–2603. <https://doi.org/10.1016/J.NANO.2017.07.008>.
- Schwabl, P., 2020. Microplastics in hot water. *Nat. Food* 671–672. <https://doi.org/10.1038/s43016-020-00174-9>, 2020 111 1.
- Schwaferts, C., Niessner, R., Elsner, M., Ivleva, N.P., 2019. Methods for the analysis of submicrometer- and nanoplastic particles in the environment. *TrAC Trends Anal. Chem.* <https://doi.org/10.1016/j.trac.2018.12.014>.
- Schymanski, D., Humpf, H.U., Fürst, P., 2018. Analysis of microplastics in water by micro-Raman spectroscopy: release of plastic particles from different packaging into mineral water. *Water Res.* 129, 154–162. <https://doi.org/10.1016/J.WATRES.2017.11.011>.
- Shard, A.G., 2020. Practical guides for X-ray photoelectron spectroscopy: quantitative XPS. *J. Vac. Sci. Technol. A* 38, 041201. <https://doi.org/10.1116/1.5141395>.
- Shruti, V.C., Pérez-Guevara, F., Elizalde-Martínez, I., Kutralam-Muniasamy, G., 2021. Current trends and analytical methods for evaluation of microplastics in stormwater. *Trends Environ. Anal. Chem.* 30, e00123. <https://doi.org/10.1016/J.TEAC.2021.E00123>.
- Snyder, R.G., Hsu, S.L., Krimm, S., 1978. Vibrational spectra in the C-H stretching region and the structure of the polymethylene chain. *Spectrochim. Acta Part A Mol. Spectrosc.* 34, 395–406. [https://doi.org/10.1016/0584-8539\(78\)80167-6](https://doi.org/10.1016/0584-8539(78)80167-6).
- Strobl, G.R., Hagedorn, W., 1978. Raman spectroscopic method for determining the crystallinity of polyethylene. *J. Polym. Sci. Polym. Phys. Ed.* 16, 1181–1193. <https://doi.org/10.1002/POL.1978.180160704>.
- Ter Halle, A., Jeanneau, L., Martignac, M., Jardé, E., Pedrono, B., Brach, L., Gigault, J., 2017. Nanoplastic in the North Atlantic subtropical gyre. *Environ. Sci. Technol.* 51, 13689–13697. <https://doi.org/10.1021/acs.est.7b03667>.
- Tomba, J.P., Silva, L.I., Genga, M.G., Galland, G.B., Perez, C.J., 2019. Characterizing chemical composition of polyolefin-based copolymers from spectral features in the C-H stretching region. *J. Raman Spectrosc.* 50, 576–586. <https://doi.org/10.1002/JRS.5554>.
- Valsesia, A., Quarato, M., Ponti, J., Fumagalli, F., Gilliland, D., Colpo, P., 2021. Combining microcavity size selection with Raman microscopy for the characterization of Nanoplastics in complex matrices. *Sci. Rep.* 11 <https://doi.org/10.1038/s41598-020-79714-z>.

- Veitmann, M., Jumeau, R., Bourson, P., Ferriol, M., Lahure, F., 2014. Understanding and control of high temperature oxidation flaws of low-density poly(ethylene) with raman spectroscopy. *Int. J. Spectrosc.* 2014, 1–9. <https://doi.org/10.1155/2014/194563>.
- Villa, S., Sanvito, T., Paroli, B., Pullia, A., Delmonte, B., Potenza, M.A.C., 2016. Measuring shape and size of micrometric particles from the analysis of the forward scattered field. *J. Appl. Phys.* 119 <https://doi.org/10.1063/1.4953332>.
- Weisser, J., Beer, I., Hufnagl, B., Hofmann, T., Lohninger, H., Ivleva, N.P., Glas, K., 2021. From the well to the bottle: identifying sources of microplastics in mineral water. *Water* 13, 841. <https://doi.org/10.3390/W13060841>, 2021Page 841 13.
- Winkler, A., Santo, N., Ortenzi, M.A., Bolzoni, E., Bacchetta, R., Tremolada, P., 2019. Does mechanical stress cause microplastic release from plastic water bottles? *Water Res.* 166, 115082 <https://doi.org/10.1016/J.WATRES.2019.115082>.
- Zhang, D., Shen, Y.R., Somorjai, G.A., 1997. Studies of surface structures and compositions of polyethylene and polypropylene by IR+visible sum frequency vibrational spectroscopy. *Chem. Phys. Lett.* 281, 394–400. [https://doi.org/10.1016/S0009-2614\(97\)01311-0](https://doi.org/10.1016/S0009-2614(97)01311-0).
- Zhang, R., Silic, M.R., Schaber, A., Wasel, O., Freeman, J.L., Sepúlveda, M.S., 2020. Exposure route affects the distribution and toxicity of polystyrene nanoplastics in zebrafish. *Sci. Total Environ.* 724, 138065 <https://doi.org/10.1016/J.SCITOTENV.2020.138065>.